



Unveiling the bifunctional modulation evoked by bromine doping of CoP towards efficient hydrolytic hydrogen generation

Chongyang Yuan^a, Tian Xu^a, Miao Guo^a, Yahui Sun^a, Tengfei Zhang^{b,*}, Xuebin Yu^{a,*}

^a Department of Materials Science, Fudan University, Shanghai 200433, China

^b Centre for Hydrogenery, College of Materials Science and Technology, Nanjing University of Aeronautics and Astronautics, Nanjing, Jiangsu 210016, China

ARTICLE INFO

Keywords:

Hydrogen generation
Catalysis
Morphology modulation
Anion doping
Electronic structure

ABSTRACT

Developing efficient and economical catalysts for hydrolytic hydrogen production from chemical hydrogen storage materials such as ammonia borane and NaBH_4 is highly desirable but challenging. Herein, Br doped CoP nanoparticles in a carbon-based polyhedron with controllable morphology were developed as such an efficient hydrogen generation catalyst, and the bifunctional modulation of Br doping was explored. Firstly, regulating the doping content of Br results in the formation of more and larger nanopores in the CoP polyhedron, exposing more accessible active sites. Secondly, Co vacancies are introduced via Br doping, which significantly optimizes the electronic structure of Co atom, thus boosting AB and water dissociation, i.e., the rate-determining step (RDS). Therefore, the Br1–CoP@C catalyst with optimal composition exhibited a superb turnover frequency (TOF) of 67.3 min^{-1} , implying an astonishing over 3-fold improvement compared with CoP@C. These findings showcase a novel and promising approach to build high-efficiency nanocatalysts for hydrogen production and beyond.

1. Introduction

With the rising demand for clean energy sources, the fuel–cell–based hydrogen economy is drawing increasing attention worldwide as a prolonged option for future energy security [1–3]. One of the greatest challenges is to discover and develop novel hydrogen storage materials with efficient H_2 storage and release performance in support of fuel–cell–based technology [4]. In recent times, because of its remarkable safety and convenience, liquid chemical hydrogen storage has become an achievable solution to realize hydrogen applications [5]. Ammonia borane (NH_3BH_3 , AB), with strengths of favorable stability, nontoxicity, and unique high hydrogen storage capacity (19.6 wt %), is a prospective liquid–phase chemical hydrogen storage reagent for hydrogen applications [6–8]. AB complex produce high purity hydrogen through pyrolysis or hydrolysis [9,10]. Compared with pyrolysis, the AB hydrolysis process is safer with lower cost, and produces three equivalent moles of hydrogen. However, for the AB hydrolysis reaction, developing a cost-effective catalyst is essential and still a challenge [11].

Among the catalyst systems studied so far, noble metal (Pt, Pd, Rh and Ru)–based catalysts have demonstrated superior activity for AB hydrolysis reaction under mild conditions [12–14]. Nevertheless, the

high cost of noble metal has hindered their wide catalysis application, which prompted the exploration of cost-effective catalysts for AB hydrolysis. Under this circumstance, designing and developing non-noble metal catalysts with efficient catalytic performance is highly desirable [15–17]. In this regard, transition metal–based catalysts have gained increasing interest. Specially, transition metal phosphides (TMPs) are receiving extensive research efforts as potential catalysts owing to their high chemical stability, various surface functions, and adjustable electronic structure [18–20]. In 2015, Fu and co-workers first reported nanostructured Ni_2P as a catalyst for AB hydrolysis, which exhibited a moderate activity and good durability [21]. Later, the same research group demonstrated that incorporating Co atoms into the Ni_2P structure significantly promoted the interplay between the catalyst and NH_3BH_3 , and lowered the reaction active barrier; thus, the optimized $\text{Ni}_{0.7}\text{Co}_{1.3}\text{P}$ nanoparticles displayed an admirable catalytic property with a TOF value of 58.4 min^{-1} based on the amount of catalyst at room temperature [19]. Recently, this composition regulation strategy has been extended to CoP–CoO nanoheterostructure [22], polar O–Co–P site [23], B–Co–P dual-active sites [24] and other structures, and achieved remarkable improvement [25–27]. In addition to composition regulation, morphology controlling has been identified as another effective approach. Li et al. successfully improved the AB hydrolysis process by

* Corresponding authors.

E-mail addresses: zhangtengfei@nuaa.edu.cn (T. Zhang), yuxuebin@fudan.edu.cn (X. Yu).

<https://doi.org/10.1016/j.apcatb.2023.123562>

Received 9 June 2023; Received in revised form 4 October 2023; Accepted 24 November 2023

Available online 28 November 2023

0926-3373/© 2023 Elsevier B.V. All rights reserved.

designing a porous multishelled hollow structure for CoP nanocatalyst [28]. However, despite the many modification strategies applied and significant progresses achieved, TMPs still display restricted catalytic performance. Therefore, developing effective methods to further progress the catalytic properties of TMPs for AB hydrolysis and investigating the corresponding structure–activity relationships is vital and urgent.

Since cation or anion vacancies can induce a large adjustment of partial properties of nanomaterials to optimize their catalytic performance (e.g., enhancing the charge mobility and adsorption performance of reaction intermediates), defect engineering has recently emerged as a powerful protocol to develop high-performance catalysts towards many conversion reactions [29–32]. For example, Guan et al. discovered that anionic oxygen vacancies can modify Co_3O_4 catalyst towards a superior catalytic performance in NH_3BH_3 hydrolysis reaction via promoting dissociation of NH_3BH_3 and H_2O molecules on Co_3O_4 [33]. Unfortunately, to the best of our knowledge, few researchers have put efforts to understand the cation vacancy effect towards enhanced catalytic activity. Moreover, to date, cation vacancy engineering has never been employed to design catalysts for AB hydrolysis, thus demonstrating great research potentials. To create cation vacancies, substituting the constituent anions with aliovalent dopants is a commonly used method. Koketsu et al. prepared deficient TiO_2 with Ti vacancies by doping constituent F^- and OH^- anions through a solvothermal process [34]. In this regard, we thus inferred that Br^- can also be used as a monovalent dopant to tune the defect structure and enhance the properties of TMPs.

Motivated by the discussion above, we herein synthesized an unusual Br-doped CoP polyhedron with Co vacancies and controllable porous structure. It was discovered that Br doping not only induced more nanopores in the CoP polyhedron structure to expose more accessible active sites, but also formed a number of cationic cobalt vacancies to regulate the electronic structure of CoP. Therefore, the developed Br-doped CoP@C nanocatalyst exhibited superior activity with a superb TOF of 67.3 min^{-1} and a hydrogen generation rate (HGR) of $28.0 \text{ L}_{\text{H}_2} \text{ min}^{-1} \text{ g}_{\text{metal}}^{-1}$, which is more than three times that of pure CoP@C and much higher than the values reported for most TMPs in AB hydrolysis reaction. Remarkably, compared with pure CoP@C, varying the Br doping content changed the degree of performance improvement, exhibiting a volcanic type catalytic behavior. In addition, the structural characterizations and density functional theory (DFT) simulations collectively proved that the formation of cobalt vacancies evoked by Br doping optimized the charge density around Co center, hence promoting the dissociation of H_2O and NH_3BH_3 molecules, and boosting hydrogen generation from AB hydrolysis.

2. Experimental section

2.1. Preparation of ZIF–67

0.87 g $\text{Co}(\text{NO}_3)_2 \cdot 6 \text{H}_2\text{O}$ and 1.31 g 2–MeIm (2–Methylimidazole) were dissolved in 40 and 20 mL of methanol respectively to form clear solution A and B. Next, the solution B was quickly poured into the solution A. After continual stirring at 30°C for 24 h, the purple precipitates were centrifuged and washed with methanol four times and dried at 60°C under dynamic vacuum on a Schlenk line.

2.2. Preparation of Brx – CoP@C

The as-synthesized ZIF–67 was placed in a tube furnace in air, heated to 300°C with a ramp rate of 2°C min^{-1} , and maintained for 2 h to prepare oxidized ZIF–67. Then, for the synthesis of CoP@C, 1 g of NaH_2PO_2 was placed at the upstream side of the oxidized ZIF–67 (20 mg) which was at the middle of a porcelain boat. The porcelain boat was then placed in a tube furnace in Ar atmosphere, heated to 320°C with a ramp rate of 5°C min^{-1} , and maintained for 2 h to prepare CoP@C. For the synthesis of Brx – CoP@C, 10x mg of hexbromobenzene (HBB) was added together with 1 g of NaH_2PO_2 , followed by the same procedure as

described above for CoP@C.

2.3. Catalysis evaluation for AB hydrolysis

5 mg catalyst with 5 mL water were preloaded into a round-bottom flask (50 mL) and followed by an ultrasonication treatment for 20 mins. Then NaOH solution (1 M, 5 mL) containing AB (1 mmol) was rapidly injected into the flask using a gastight syringe to initiate the reaction. During the reaction process, the flask reactor was hold under stirring conditions at a certain temperature. The corresponding hydrogen generation volume was collected by a flowmeter (Ritter MGC–1 V3.4 PMMA) which was connected to a computer. The test was terminated when gas was no longer generated. The catalytic activity was evaluated by the TOF value:

$$\text{TOF} = \frac{n_{\text{H}_2}}{n_{\text{metal}} * t} \quad (1)$$

in which n_{H_2} is the mole number of generated H_2 , n_{metal} is the mole number of metal element in the catalyst, and t is the reaction time in the unit of minutes. In stability experiment, the catalyst was recovered through centrifugation with deionized water and absolute ethyl alcohol and dried under vacuum at room temperature. Then repeated experiment was conducted under the same test condition.

2.4. Material characterization

X – ray diffraction patterns (XRD) were collected through a Rigaku D/max 2000 diffractometer with monochromatized $\text{Cu K}\alpha$ radiation ($\lambda = 1.5418 \text{ \AA}$) at a scan rate of $10^\circ \text{ min}^{-1}$. X – ray photoelectron spectroscopy (XPS) was performed on a Thermo Scientific K–Alpha using 200 W monochromated $\text{Al K}\alpha$ radiation. Scanning electron microscopy (SEM) was performed on a Hitachi S–4800 electron microscope with acceleration voltage of 1 kV. Transmission electron microscopy (TEM) high-resolution TEM (HRTEM) images were taken with a Hitachi–7700 working at 100 kV. High angle annular dark-field scanning transmission electron microscopy (HAADF-STEM) and energy dispersive X – ray spectroscopy (EDX) mapping were conducted on a JEOL JEM–2100 F field emission electron microscope working at 200 kV. Spherical aberration corrected TEM image was obtained from FEI Theims Z. Inductively coupled plasma optical emission spectrometry (ICP–OES) was measured using a Thermo Fisher iCAP PRO. Transmission X – ray absorption fine structure (XAFS) measurements were conducted using a laboratory device (easyXAFS300, easyXAFS LLC), which is based on Rowland circle geometries with spherically bent crystal analyzers (SBCA) and operated using an Ag X – ray tube source and a silicon drift detector (AXAS–M1, KETEK GmbH). The nitrogen adsorption-desorption isotherms were carried out on an ASAP 2460 Micromeritics analyzer.

3. Results and discussion

3.1. Catalyst preparation and characterization

The catalyst preparation process is shown in Fig. 1a. Firstly, CoP nanoparticles in a carbon-based polyhedron framework (named CoP@C) were synthesized through a classical zeolitic imidazolate frameworks (ZIF–67) derived method. As for Br-doped CoP@C (named Brx – CoP@C, x represents the relative Br content), HBB was used as the bromine source to introduce Br into CoP during the phosphorization process of oxidized ZIF–67. Based on the valence states conservation principle, the doping of Br^- inevitably leads to the change of valence state for Co. Therefore, due to the lack of monovalent Co, it is more likely to form cationic vacancies to achieve equilibrium.[34] To further validate this result, the formation energies of different compositions were calculated by DFT computations as shown in Fig. S1. Comparing

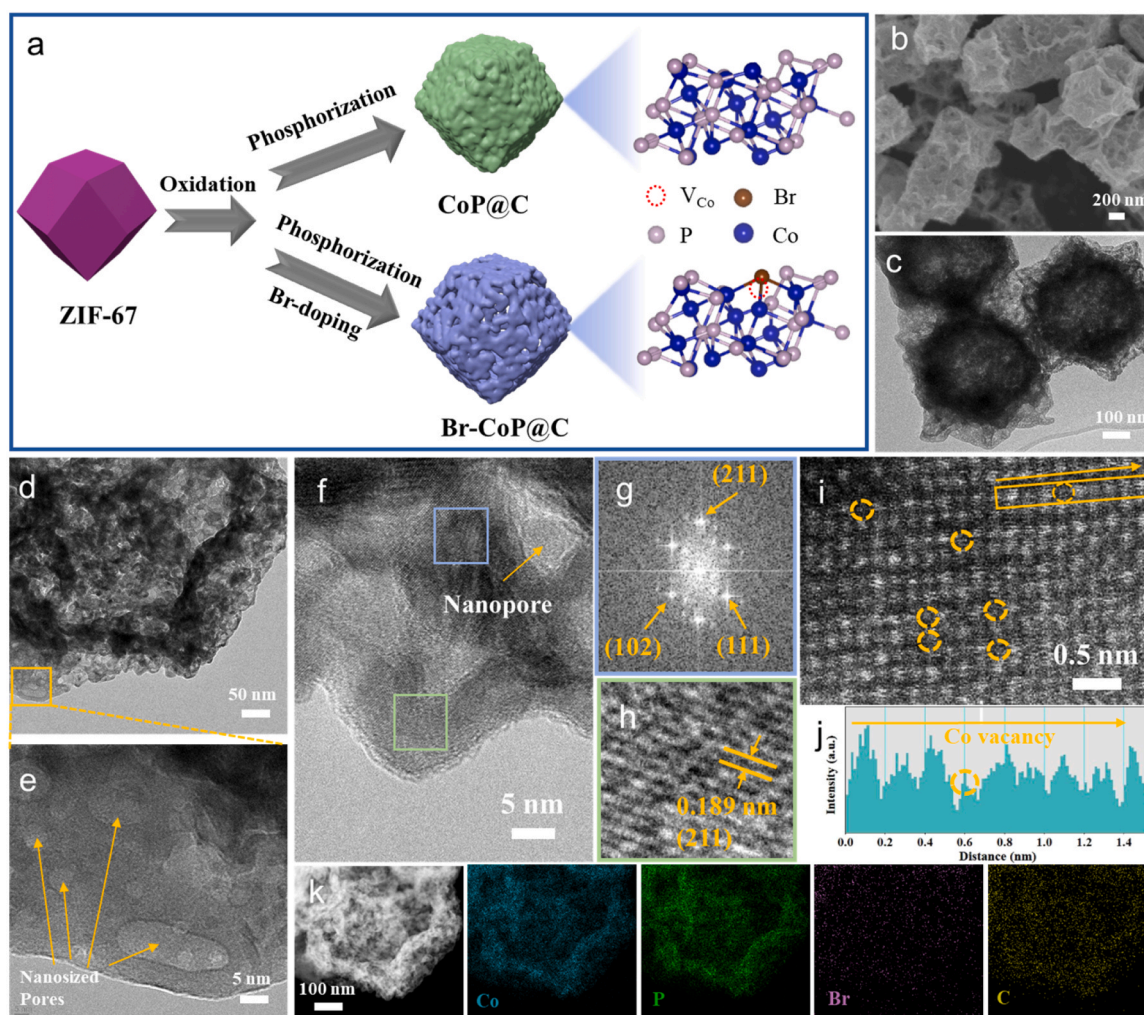


Fig. 1. The preparation process and morphology of CoP@C and Br-CoP@C catalysts. (a) Schematic fabrication process of Br-CoP@C. (b) SEM, (c, d) TEM and (e, f) HRTEM images of Br1-CoP@C. (g) Fast Fourier transform (FFT) images of the blue square in (f). (h) IFFT image of the green square in (f). (i) Aberration-corrected (AC)-HAADF-STEM image of Br1-CoP@C, in which Co vacancies are highlighted with yellow circles. (j) Intensity profile recorded for the corresponding region in (i). (k) STEM image and corresponding EDX mapping images of Br1-CoP@C.

with pristine CoP, the CoP structure with Br doping exhibits a lower formation energy. On this basis, introducing Co vacancies in the structure of Br-doped CoP further lowers the formation energy, indicating that the formation of cationic Co vacancies in CoP structure is thermodynamically stable.

The polyhedron morphologies of CoP@C and Brx-CoP@C are shown in the SEM (Fig. 1b and Fig. S2) and TEM images (Fig. 1c). More pores appear in the material with the increasing content of Br, revealing a morphology modulation effect of Br doping. Besides, as shown in Fig. S3, the Brunauer-Emmett-Teller (BET) specific surface area was conducted and showed in the order of Br1-CoP@C ($23.0 \text{ m}^2 \text{ g}^{-1}$) > CoP@C ($17.8 \text{ m}^2 \text{ g}^{-1}$), which also demonstrates the function of these nanopores. The HRTEM images also confirm the abundance of nanopores in Br1-CoP@C (Fig. 1d-f). As for CoP@C, the SEM and TEM images reveal a clear rhombic polyhedron morphology with smooth surface and uniform size (Fig. S4). However, no nanopores can be observed in the HRTEM images (Fig. S4d, f). These results clearly indicate that the introduction of Br can effectively modulate the morphology of CoP@C polyhedron. It seems that Br doping can increase the specific surface area of CoP through an effective pore-making approach, which is favorable for exposing more metal active sites and facilitating the catalysis application.

In addition, HRTEM images (Fig. 1f-h and Fig. S4d) also

demonstrate that Br1-CoP@C presents the (211) planes of CoP with the lattice spacing of 0.189 nm. The regions in blue and green boxes were subjected to fast Fourier transform and inverse fast Fourier transform to clearly show more details about the crystal structure (Fig. 1g). The diffraction patterns of (102), (111) and (211) planes can be clearly identified. To confirm the existence of defects, the atomic-resolution HAADF-STEM was carried out and directly revealed the cationic Co vacancies as marked with yellow circles (Fig. 1i). Besides, the intensity profile collected for the corresponding region in Fig. 1j indicates atomic arrangement of Co atoms, revealing that some Co atoms are missing and confirming the presence of Co vacancies. In contrast, completely crystalline regions with no vacancies are observed from the atomic-resolution HAADF-STEM image (Fig. S4e) of the Fourier transformed pattern of CoP@C, which validates the important role of Br doping for defect formation and is also consistent with the theoretical prediction. The electron paramagnetic resonance (EPR) signals for Br1-CoP@C with the g-value of 2.004 further confirm the existence of Co vacancies; and in comparison, there is no obvious signal for CoP@C (Fig. S5). These results verify the presence of unpaired electrons produced by Co defects in Br1-CoP@C, which can markedly promote the adsorption and decomposition of AB and H₂O molecules [39]. In addition, HAADF-STEM images and EDX mapping in Fig. 1k present that the Co, P, Br, and C are uniformly distributed throughout the Br1-CoP@C

polyhedron, suggesting that Br element is successfully introduced.

XRD patterns of CoP@C and Brx – CoP@C are displayed in Fig. 2a. Both patterns are consistent with the standard JCPDS No. 29-0497, and the diffraction peaks at 31.7° , 36.4° , and 48.2° are attributed to the (011), (111) and (211) crystal faces of CoP, respectively. This indicates that Br1 – CoP@C maintains the original crystal structure after Br doping, implying the successful incorporation of bromine. Further, XPS measurement was conducted to probe the changes in the electronic state of CoP after Br doping. The Co 2p spectrum of Br1 – CoP@C (Fig. 2b) displays two peaks of Co $2p_{1/2}$ at 792.7 and 797.2 eV as well as two peaks of Co $2p_{3/2}$ at 778.1 and 781.0 eV, corresponding to Co^{3+} and Co^{2+} , respectively [35–37]. Compared with CoP@C, the binding energy of the Co 2p spectrum of Br1 – CoP@C is decreased by 0.3 eV, suggesting that Br doping changes the electronic structure of Co. The binding energy of P $2p_{1/2}$ and P $2p_{3/2}$, which is located at 130.0 and 129.3 eV, respectively, is revealed in the P 2p spectrum of Br1 – CoP@C (Fig. 2f) [36,38]. The relatively wide peak around 134.0 eV can be

triggered by P–O species due to surface oxidation. It should also be noted that the P 2p peaks of Br1 – CoP@C shift positively to higher binding energies in contrast to pure CoP@C, signifying a reduced electron density of P atoms. Hence, the introduction of Br modulates the electronic structure of CoP through charge transformation from P atoms to Co atoms. Thus, Br doping induces clear electronic differences. Furthermore, the peak at 68.6 eV belongs to the Co–Br bond in the Br 3d spectrum of Br1 – CoP@C, which is completely different from the Br 3d peaks of the C–Br bond in HBB (Figs. 2d, S6), indicating the successful doping of Br and coupling of Br with Co [40].

XAFS spectras were conducted to further clarify the local geometric structure and electronic structure of Br1 – CoP@C. Fig. 2e and Fig. S7 show the Co K-edge X-ray absorption near edge structure (XANES) results of Co foil, Co_3O_4 , CoP@C and Br1 – CoP@C. The absorption edges of Br1 – CoP@C and CoP@C are sandwiched between Co foil and Co_3O_4 (Fig. S7), agreeing with literature reports and confirming the formation of CoP phase [40]. Additionally, after Br doping, the

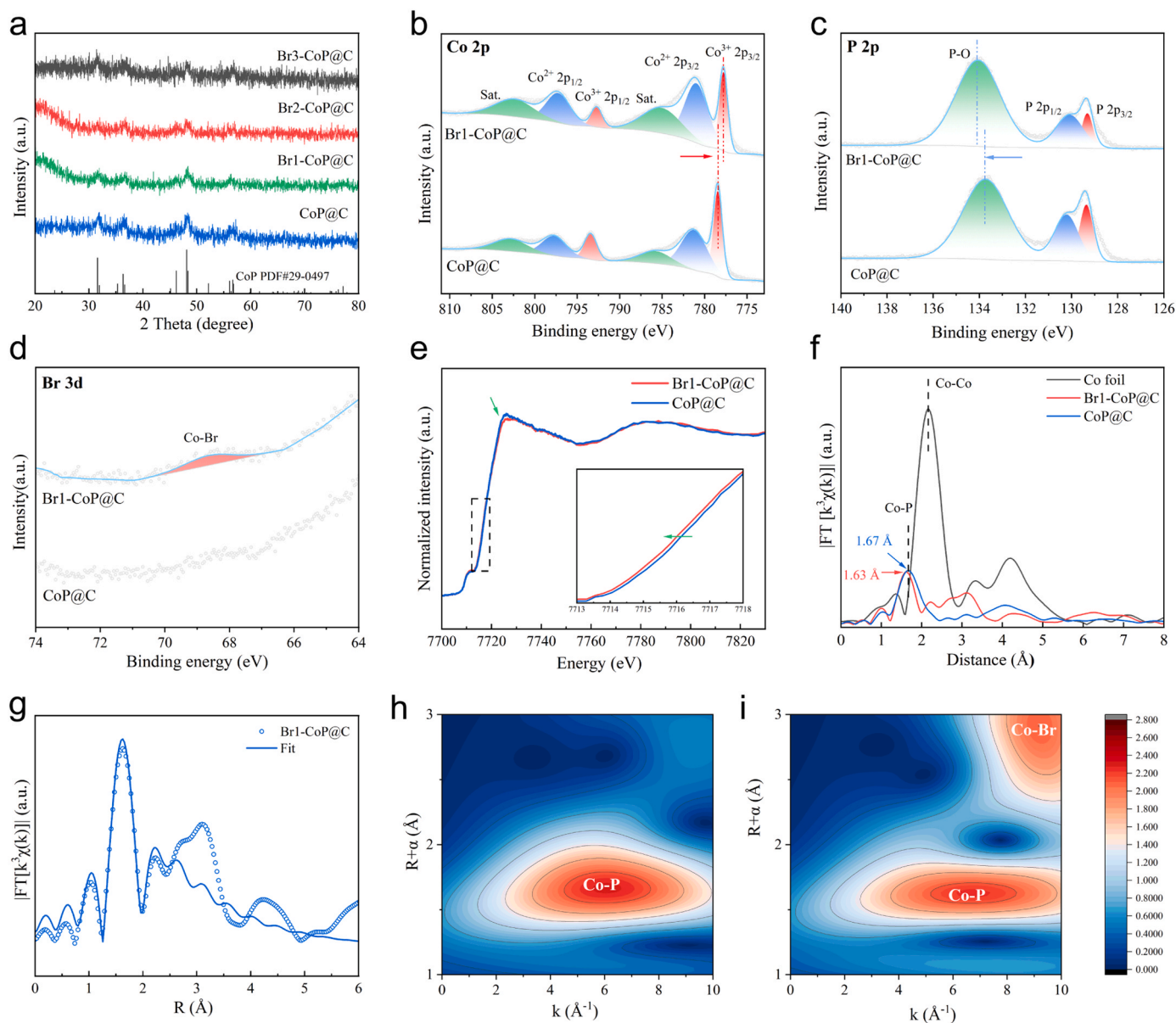


Fig. 2. Structural characterization of CoP@C and Br–CoP@C catalysts. (a). XRD patterns of CoP@C and Brx – CoP@C. High resolution XPS of (b) Co 2p, (c) P 2p and (d) Br 3d of CoP@C and Br1 – CoP@C. (e) Normalized XANES spectra of the Co K-edge of CoP@C and Br1 – CoP@C. (f) Fourier transform of the Co K-edge EXAFS of Co foil, CoP@C and Br1 – CoP@C. (g) Co K-edge EXAFS fitting curves of Br1 – CoP@C in R-space. Wavelet transform plots of Co K-edge in (h) CoP@C and (i) Br1 – CoP@C.

pre-edge of Co decreases to a lower energy value and the intensity of the white line is mildly diminished as shown in Fig. 2e. This is caused by the increased electron density of Co atom due to Br incorporation, which is consistent with XPS analyses. The K-edge extended X-ray absorption fine structure (EXAFS) oscillations of Co in Fig. 2f presents the typical peak of Co–P bond at around 1.65 Å. Demonstrably, small amplitude means low coordination number and large disorder, and the peak strength for Co–P bond in Br1–CoP@C is slightly smaller than that in CoP@C, thus representing a decrease in the coordination number between Co and P after introducing Co vacancies [41]. The wavelet transform plots (Figs. 2h, 2i) also confirm the change of Co–P coordination number in Br1–CoP@C with a slightly lower intensity of Co–P bond (around $k = 6 \text{ \AA}^{-1}$) observed. Furthermore, data fitting results visually show the reduction of the Co–P coordination number from 4.5 to 3.6 (Table S2, Fig. 2g and Fig. S8), which corroborates the previous conclusion. Concurrently, the above results powerfully prove the formation of cationic Co vacancies in Br1–CoP@C.

3.2. Catalytic performance evaluation

The hydrogen generation curves of the catalytic AB hydrolysis process were evaluated by employing a gas flowmeter and the catalytic hydrogen generation performance is presented in Fig. 3. The catalytic performances of Brx–CoP@C catalysts with various Br doping contents are shown in Fig. 3a and Fig. S10. The rates of hydrogen evolution from the hydrolysis reaction are in this order: Br1–CoP@C > Br3–CoP@C > Br2–CoP@C > CoP@C. Among all the catalysts, Br1–CoP@C exhibits the highest hydrogen evolution rate, with a TOF value of 67.3 min^{-1} which is determined by the metal dosage for catalyzing complete reaction (Fig. 3b). This TOF value is over 3 times that of the pure CoP@C catalyst (20.4 min^{-1}) and superior than most catalysts previously reported. It is worth noting that the evaluated catalytic properties of Brx–CoP@C catalysts show a volcano-like behavior with the increasing Br content, revealing that Br doping plays a crucial part in promoting the catalytic activity of CoP for hydrolytic hydrogen generation from AB.

Additionally, the vital role of Br doping has been demonstrated for

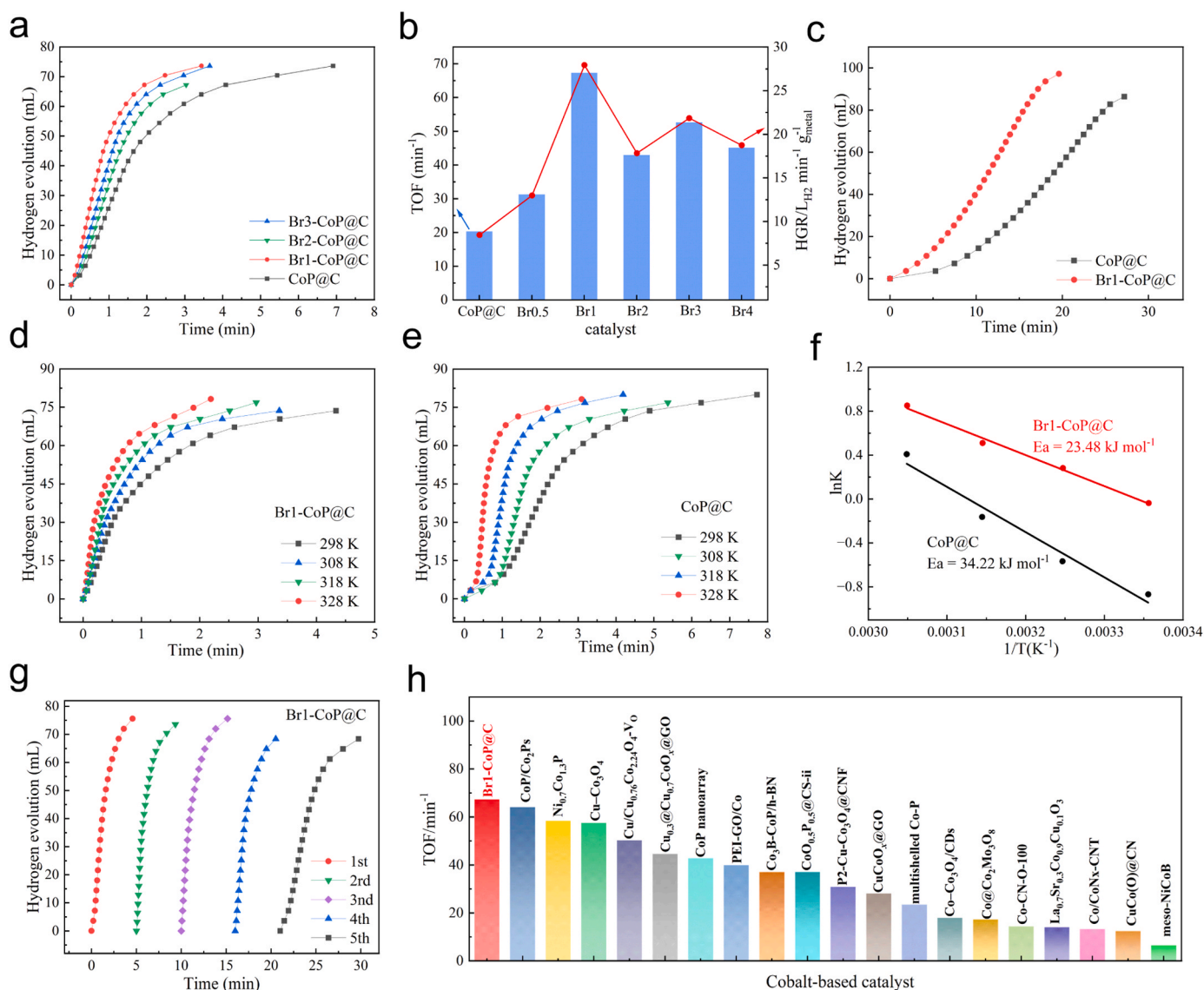


Fig. 3. Hydrogen evolution curves from AB hydrolysis catalyzed by (a) CoP@C, Br1–CoP@C, Br2–CoP@C and Br3–CoP@C at 298 K with (b) the corresponding HGR and TOF values. (c) Hydrogen evolution curves from NaBH_4 hydrolysis catalyzed by CoP@C and Br1–CoP@C at 298 K. Hydrogen production from AB hydrolysis catalyzed by (d) CoP@C and (e) Br1–CoP@C at diverse temperatures with (f) the corresponding Arrhenius plots. (g) Cyclic stability test of Br1–CoP@C at 298 K. (h) TOF values of Br1–CoP@C and other reported Co-based catalysts.

NaBH_4 hydrolysis. As shown in Fig. 3c, the hydrolysis reaction of 1 mmol NaBH_4 completes within 19 mins under the function of Br1 –CoP@C, while less than 90 % NaBH_4 conversion is reached within 30 mins by pure CoP@C. However, compared with their actions on AB conversion, the catalysts are less effective for NaBH_4 hydrolysis. This could be attributed to the molecular geometry difference between NaBH_4 and NH_3BH_3 which affects the catalytic behavior. Fig. 3d–f illustrates the catalytic hydrogen evolution performance by CoP@C and Br1 –CoP@C catalysts for AB hydrolysis at different temperatures. As the reaction temperature rises, the hydrogen evolution performance gains a significantly enhancement. Specifically, elevating the temperature to 328 K, the TOF value of Br1 –CoP@C increases to 177.9 min^{-1} , elucidating a calculated apparent activation energy of $23.48 \text{ kJ mol}^{-1}$. In contrast, the calculated activation energy with CoP@C as the catalyst is $34.22 \text{ kJ mol}^{-1}$, which is considerably higher than that for Br1 –CoP@C-catalyzed reaction, verifying that introducing Co vacancies into CoP can further reduce the activation energy barrier of AB hydrolysis. The activation energy value under the catalysis of Br1 –CoP@C also has certain competitive advantages over some reported metal catalysts (Table S3).

The cyclic stability is another essential factor for catalyst evaluation, thus the cycle measurements of Br1 –CoP@C were executed. As illustrated in Fig. 3g, it is discovered that its activity for hydrogen release remained pretty stable after 4 cycles, indicating the decent cyclic stability of Br1 –CoP@C. However, a gradual decrease in the catalytic activity is observed in last cycle, which is probably because of the deactivation of the catalysts by the B-containing species after a long time reaction [42,43]. The above results validate the efficient catalyst activity of Br1 –CoP@C. Further, the catalytic activities of the Co-based catalysts and other transition metals catalysts were compared. Br1 –CoP@C demonstrates a superior catalytic performance and its TOF value is higher than those of most reported materials in literature (Fig. 3h and Table S3).

3.3. Mechanism insights

Understanding the relationship between catalytic performance and catalyst structure is of great importance to guide reasonable design of catalysts. The kinetic experiments were first conducted over the Br1 –CoP@C catalyst. The hydrogen generation rate remains relatively unchanged as the substrate concentration varies, suggesting the irrelevance between the hydrolysis reaction rate and AB concentration over Br1 –CoP@C, in line with literatures (Fig. S11). By contrast, the concentration of catalyst significantly affects the hydrogen generation rate (Fig. S12, slope of the logarithmic plot with 1.00), following the first-order reaction kinetics, which means there is no mass transfer problem during the catalytic process [44–46].

In addition, a kinetic isotope effect (KIE) value of 2–7 is defined as the primary kinetic isotope effect, generally indicating the formation and breaking of bonds to the isotopically labelled atom in the RDS [47]. The KIE was also examined on CoP@C and Br1 –CoP@C to identify the RDS. When D_2O was used as a reactant instead of H_2O , the hydrogen evolution rate catalyzed by Br1 –CoP@C dropped to 23.1 min^{-1} , implying a KIE value of 2.91. This value clarifies that the RDS of AB hydrolytic hydrogen generation is the splitting of water molecule (Fig. 4a), which agrees with former reports [19,48]. A similar result was also obtained for CoP@C, but with a higher KIE value of 3.11 (Fig. 4c), indicating that Br1 –CoP@C is more efficient than CoP@C for activating water molecules on account of the modification by Co vacancies.

To gain deep insights into the catalytic mechanism over the CoP structure with Br doping, comprehensive DFT calculations were carried out. According to the XRD and HRTEM results, the exposed (211) lattice plane with high-index was filtered as the active surface. To begin with, the cleavage process of H_2O was estimated on the CoP and Br–CoP catalyst models (Fig. 4b) and the simulated three-dimensional (3D) structures of adsorbed H_2O (H_2O^*), transition state (TS) and end products ($\text{OH}^* + \text{H}^*$) are shown in Fig. S13. It is found that the water

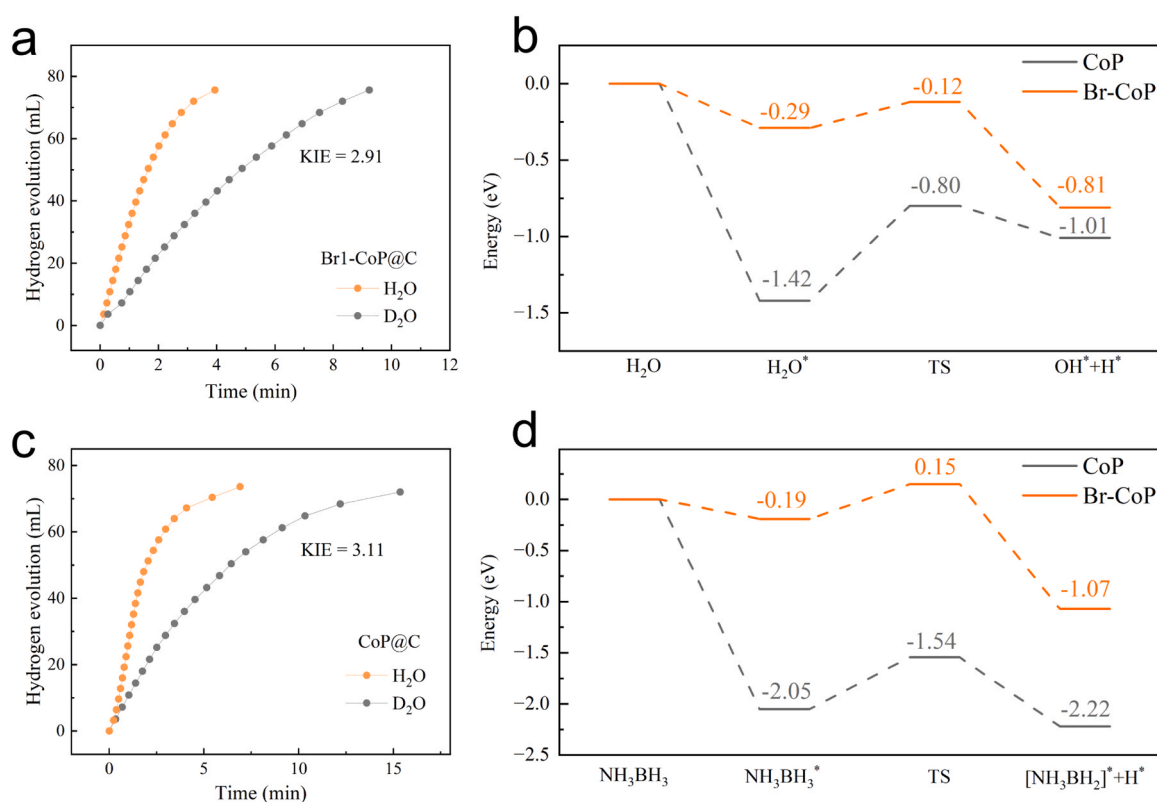


Fig. 4. Hydrogen evolution curves from AB hydrolysis with H_2O and D_2O catalyzed by (a) Br1 –CoP@C and (c) CoP@C at 298 K. Energy profiles of (b) H_2O dissociation and (d) B–H bond dissociation in NH_3BH_3 on the CoP (211) and Br–CoP (211) slabs.

molecules could be favorably chemisorbed on the catalyst model via the $\text{H}_2\text{O}\cdots\text{Co}$ interaction with the Br doped CoP (211) plane, which is featured by an exothermic energy of 0.29 eV. Afterwards, the dissociation of O–H bond is evaluated with a corresponding energy barrier of 0.17 eV. By contrast, Fig. 4b displays a similar water dissociation on the pure CoP (211) plane, and the simulated results show that the energy barrier of H_2O activation on the CoP (211) plane is 0.62 eV, which is much higher than that on the Br–CoP (211) model. A similar promotion effect of Co vacancy in the AB chemisorption process could also be found by the computational simulation. The energy profile of B–H bond cleavage in NH_3BH_3 on the Br–CoP (211) plane is shown in Fig. 4d and Fig. S14, with an energy barrier of 0.34 eV. On the contrary, the B–H bond dissociates more slowly on the CoP (211) plane with a higher energy barrier of 0.51 eV compared with that on Br–CoP (Fig. 4d), which means that the Br–CoP (211) model achieves higher efficiency for catalyzing the breaking of B–H bond in NH_3BH_3 . Therefore, the kinetic experiments and DFT calculations comprehensively demonstrate that the existence of Co vacancy can boost both the breakage of O–H bond and B–H bond so that the Br1–CoP@C performs a superior catalytic activity.

The projected density of states (DOS) supplementary recognizes the modification of the electronic structure of CoP via Br–doping and Co vacancy (here after named V_{Co}). As displayed in Fig. S15, after Br doping into CoP, the d–band center of CoP upshifts to -1.19 eV. Based on the d–band center theory, more antibonding states will be formed upon a decrease of the d–band center, resulting in reduced bond strength [49]. Thus, the higher d band center signifies a stronger adsorption strength towards both H_2O and H^* on Br–CoP than that on CoP [50]. The strong adsorption strength of H_2O on Br–CoP may elongate the H–O bond of adsorbed H_2O and thus facilitate H_2O dissociation. Moreover, the charge density analysis suggests that the involvement of Br and V_{Co} results in a strong local charge redistribution around Co atoms (Fig. 5b). To be specific, though the V_{Co} can directly decrease the charge density of several Co atoms around it, the Br and P atoms with high charge density will convert their charge to Co atoms, giving rise to the finally increased charge density of Co atoms, as seen in Fig. 5b. This is in line with the characterization results. Combining the nanopore–making effect of Br doping as mentioned above (Fig. 5a), the systematical experiments and calculations evidenced that the Br and V_{Co} introduction could significantly and favorably modulate the morphology and electronic structure of CoP, leading to an enhanced catalytic activity for efficient hydrolytic dehydrogenation.

4. Conclusion

In summary, we have successfully introduced cationic Co vacancies into CoP polyhedron matrix through a Br anion doping strategy and explored the correlation between the structure change and the promoted catalytic performance. Comprehensive DFT and spectroscopic characterization reveals that Br introduction could lead to the formation of Co vacancies and greatly affect the catalytic performance of CoP via a bifunctional modulation effect. Firstly, Br doping content can directly regulate the number and area of nanopores formed in the CoP polyhedron matrix, eventually demonstrating an increased specific area and more exposed active sites. Secondly, the introduced Co vacancies can significantly increase the charge density of Co center in CoP, resulting in the increasing of adsorption energy of H_2O and decreasing of dissociation energy of H_2O and AB, thus cooperatively boosting hydrogen production. According to the two points above, the morphology modulation and electronic structure optimization synergistically improve the catalytic activity of CoP for NH_3BH_3 hydrolysis, leading to a superior TOF of 67.3 min^{-1} which is a more than 3–fold enhancement compared with pure CoP before Br doping. In short, the current findings unveil the crucial roles of the electronic structure of active site center at an atomic level in TMPs, endowing guidance for developing novel robust nanocatalysts in hydrolytic hydrogen evolution and beyond.

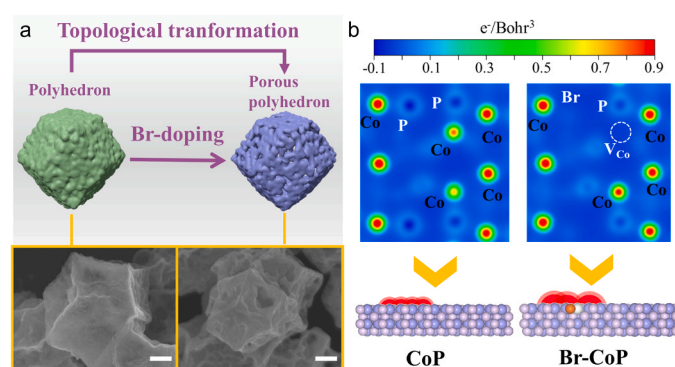


Fig. 5. The morphological and electronic dual modulation of Br–doping. (a) Schematic illustration of topological transformation from polyhedron (CoP@C) to porous polyhedron (Br1–CoP@C) with corresponding sample SEM images, scale bar: 100 nm. (b) Charge density analyses of CoP and Br–CoP with corresponding 3D structures. The balls in light purple, dark purple, orange and white represent P, Co, Br, and V_{Co} , respectively.

CRediT authorship contribution statement

Chongyang Yuan: Investigation, Formal analysis, Data curation, Writing – original draft. **Tian Xu:** Data curation, Software, Writing – original draft. **Miao Guo:** Investigation, Formal analysis. **Yahui Sun:** Review & Editing. **Tengfei Zhang:** Investigation, Formal analysis, Writing – review & editing, Funding acquisition. **Xuebin Yu:** Conceptualization, Writing – review & editing, Supervision, Funding acquisition.

Declaration of Competing Interest

The authors declare that they have no known competing financial interests or personal relationships that could have appeared to influence the work reported in this paper.

Data availability

Data will be made available on request.

Acknowledgements

This work was partially supported by the National Key R&D Program of China (No. 2020YFA0406204), the National Natural Science Foundation of China (51971065, 52171180, 51802154, and 22109026), the Innovation Program of Shanghai Municipal Education Commission (2019–01–07–00–07–E00028), the Fundamental Research Funds for the Central Universities (NG2022005), and the Scientific and Technological Innovation Special Fund for Carbon Peak and Carbon Neutrality of Jiangsu Province (No. BK20220039).

Appendix A. Supporting information

Supplementary data associated with this article can be found in the online version at [doi:10.1016/j.apcatb.2023.123562](https://doi.org/10.1016/j.apcatb.2023.123562).

References

- [1] L. Schlapbach, A. Züttel, Hydrogen-storage materials for mobile applications, *Nature* 414 (2001) 353–358, <https://doi.org/10.1038/35104634>.
- [2] M.S. Dresselhaus, I.L. Thomas, Alternative energy technologies, *Nature* 414 (2001) 332–337, <https://doi.org/10.1038/35104599>.
- [3] L. Van Hoecke, L. Laffineur, R. Campe, P. Perreault, S.W. Verbruggen, S. Lenaerts, Challenges in the use of hydrogen for maritime applications, *Energy Environ. Sci.* 14 (2021) 815–843, <https://doi.org/10.1039/d0ee01545h>.
- [4] M.D. Allendorf, V. Stavila, J.L. Snider, M. Witman, M.E. Bowden, K. Brooks, B. L. Tran, T. Autrey, Challenges to developing materials for the transport and storage

- of hydrogen, *Nat. Chem.* 14 (2022) 1214–1223, <https://doi.org/10.1038/s41557-022-01056-2>.
- [5] P.P. Edwards, V.L. Kuznetsov, W.I.F. David, N.P. Brandon, Hydrogen and fuel cells: towards a sustainable energy future, *Energy Policy* 36 (2008) 4356–4362, <https://doi.org/10.1016/j.enpol.2008.09.036>.
 - [6] Y. Zhu, L. Ouyang, H. Zhong, J. Liu, H. Wang, H. Shao, Z. Huang, M. Zhu, Closing the loop for hydrogen storage: facile regeneration of NaBH_4 from its hydrolytic product, *Angew. Chem. Int. Ed.* 59 (2020) 8623–8629, <https://doi.org/10.1002/anie.201915988>.
 - [7] Q. Sun, N. Wang, Q. Xu, J. Yu, Nanopore-supported metal nanocatalysts for efficient hydrogen generation from liquid-phase chemical hydrogen storage materials, *Adv. Mater.* 32 (2020), e2001818, <https://doi.org/10.1002/adma.202001818>.
 - [8] L. Ouyang, J. Jiang, K. Chen, M. Zhu, Z. Liu, Hydrogen production via hydrolysis and alcoholysis of light metal-based materials: a review, *Nano Micro Lett.* 13 (2021), 134, <https://doi.org/10.1007/s40820-021-00657-9>.
 - [9] T.B. Marder, Will we soon be fueling our automobiles with ammonia–borane? *Angew. Chem. Int. Ed.* 46 (2007) 8116–8118, <https://doi.org/10.1002/anie.200703150>.
 - [10] C. Wang, Q. Wang, F. Fu, D. Astruc, Hydrogen generation upon nanocatalyzed hydrolysis of hydrogen-rich boron derivatives: recent developments, *Acc. Chem. Res.* 53 (2020) 2483–2493, <https://doi.org/10.1021/acs.accounts.0c00525>.
 - [11] C. Wang, D. Astruc, Recent developments of nanocatalyzed liquid-phase hydrogen generation, *Chem. Soc. Rev.* 50 (2021) 3437–3484, <https://doi.org/10.1039/D0CS00515K>.
 - [12] W.-W. Zhan, Q.-L. Zhu, Q. Xu, Dehydrogenation of ammonia borane by metal nanoparticle catalysts, *ACS Catal.* 6 (2016) 6892–6905, <https://doi.org/10.1021/acscatal.6b02209>.
 - [13] J. Zhang, W. Yu, D. Feng, H. Xu, Y. Qin, Porous titania nanotube confined ultrafine platinum catalysts synthesized by atomic layer deposition with enhanced hydrolytic dehydrogenation performance, *Appl. Catal. B* 312 (2022), 121405, <https://doi.org/10.1016/j.apcatb.2022.121405>.
 - [14] S. Zhou, Y. Yang, P. Yin, Z. Ren, L. Wang, M. Wei, Metal-support synergistic catalysis in $\text{Pt}/\text{MoO}_{3-x}$ nanorods toward ammonia borane hydrolysis with efficient hydrogen generation, *ACS Appl. Mater. Interfaces* 14 (2022) 5275–5286, <https://doi.org/10.1021/acsami.1c20736>.
 - [15] Q. Yao, Y. Ding, Z.-H. Lu, Noble-metal-free nanocatalysts for hydrogen generation from boron- and nitrogen-based hydrides, *Inorg. Chem. Front.* 7 (2020) 3837–3874, <https://doi.org/10.1039/d0qi00766h>.
 - [16] Y.-Z. Yang, L.-Q. Zhao, X.-Y. Gao, Y.-F. Zhao, Constructing ultrafine monodispersed $\text{Co}_2\text{P}/(0.59\text{-Cu}_3\text{P})$ on Cu doped CoZn-ZIF derived porous N-doped carbon for highly efficient dehydrogenation of ammonia borane, *Nano Res.* 16 (2023) 6687–6700, <https://doi.org/10.1007/s12274-023-5463-y>.
 - [17] S. Guan, Y. Liu, H. Zhang, H. Wei, T. Liu, X. Wu, H. Wen, R. Shen, S. Mehdi, X. Ge, C. Wang, B. Liu, E. Liang, Y. Fan, B. Li, Atomic interface-exciting catalysis on cobalt nitride-oxide for accelerating hydrogen generation, *Small* 18 (2022), e2107417, <https://doi.org/10.1002/smll.202107417>.
 - [18] C.D. Mboiyi, D. Poinso, J. Roger, K. Fajferwer, M.L. Kahn, J.C. Hierro, The hydrogen-storage challenge: nanoparticles for metal-catalyzed ammonia borane dehydrogenation, *Small* 17 (2021), e2102759, <https://doi.org/10.1002/smll.202102759>.
 - [19] C.-C. Hou, Q. Li, C.-J. Wang, C.-Y. Peng, Q.-Q. Chen, H.-F. Ye, W.-F. Fu, C.-M. Che, N. Lopez, Y. Chen, Ternary Ni-Co-P nanoparticles as noble-metal-free catalysts to boost the hydrolytic dehydrogenation of ammonia-borane, *Energy Environ. Sci.* 10 (2017) 1770–1776, <https://doi.org/10.1039/c7ee01553d>.
 - [20] C. Wan, X.L. Liu, J.P. Wang, F.Q. Chen, D.G. Cheng, Heterostructuring 2D Co_2P nanosheets with OD CoP via a salt-assisted strategy for boosting hydrogen evolution from ammonia borane hydrolysis, *Nano Res.* 16 (2023) 6260–6269, <https://doi.org/10.1007/s12274-023-5388-5>.
 - [21] C.-Y. Peng, L. Kang, S. Cao, Y. Chen, Z.-S. Lin, W.-F. Fu, Nanostructured Ni_2P as a robust catalyst for the hydrolytic dehydrogenation of ammonia–borane, *Angew. Chem. Int. Ed.* 54 (2015) 15725–15729, <https://doi.org/10.1002/anie.201508113>.
 - [22] H. Wu, Y. Cheng, B. Wang, Y. Wang, M. Wu, W. Li, B. Liu, S. Lu, Carbon dots-confined CoP-CoO nanoheterostructure with strong interfacial synergy triggered the robust hydrogen evolution from ammonia borane, *J. Energy Chem.* 57 (2021) 198–205, <https://doi.org/10.1016/j.ijechem.2020.08.051>.
 - [23] H. Zhang, K. Zhang, S. Ashraf, Y. Fan, S. Guan, X. Wu, Y. Liu, B. Liu, B. Li, Polar O-Co-P surface for bimolecular activation in catalytic hydrogen generation, *Energy Environ. Mater.* 6 (2022), e12273, <https://doi.org/10.1002/eeem2.12273>.
 - [24] H. Zhang, Y. Liu, H. Wei, C. Wang, T. Liu, X. Wu, S. Ashraf, S. Mehdi, S. Guan, Y. Fan, X. Yue, B. Liu, Y. Zhang, H. Cao, B. Li, Atomic-bridge structure in B-Co-P dual-active sites on boron nitride nanosheets for catalytic hydrogen generation, *Appl. Catal., B* 314 (2022), 121495, <https://doi.org/10.1016/j.apcatb.2022.121495>.
 - [25] Y. Chen, K. Peng, G. Yuan, Z. Kang, J. Zhong, Highly efficient CoNiP nanoboxes on graphene oxide for the hydrolysis of ammonia borane, *Chem. Eng. J.* 428 (2022), 131219, <https://doi.org/10.1016/j.cej.2021.131219>.
 - [26] C. Wang, L. Cheng, S. Ye, P. Yan, L. Sun, Aerogel of chitosan/graphene oxide loaded Ru-CoP as a monolithic catalyst for hydrogen generation via NaBH_4 hydrolysis, *J. Alloy. Compd.* 952 (2023), 169994, <https://doi.org/10.1016/j.jallcom.2023.169994>.
 - [27] L.J. Zhang, J. Ye, Y. Tu, Q.Y. Wang, H.B. Pan, L.H. Wu, X.S. Zheng, J.F. Zhu, Oxygen modified CoP_2 supported palladium nanoparticles as highly efficient catalyst for hydrolysis of ammonia borane, *Nano Res.* 15 (2022) 3034–3041, <https://doi.org/10.1007/s12274-021-3941-7>.
 - [28] P. Li, Y.Q. Huang, Q.H. Huang, R. Chen, J.X. Li, S.H. Tian, Cobalt phosphide with porous multishelled hollow structure design realizing promoted ammonia borane dehydrogenation: elucidating roles of architectural and electronic effect, *Appl. Catal. B* 313 (2022), 121444, <https://doi.org/10.1016/j.apcatb.2022.121444>.
 - [29] R. Zhang, L. Pan, B. Guo, Z.F. Huang, Z. Chen, L. Wang, X. Zhang, Z. Guo, W. Xu, K. P. Loh, J.J. Zou, Tracking the role of defect types in Co_3O_4 structural evolution and active motifs during oxygen evolution reaction, *J. Am. Chem. Soc.* 145 (2023) 2271–2281, <https://doi.org/10.1021/jacs.2c10515>.
 - [30] Z. Li, Y. Zhou, M. Xie, H. Cheng, T. Wang, J. Chen, Y. Lu, Z. Tian, Y. Lai, G. Yu, High-density cationic defects coupling with local alkaline-enriched environment for efficient and stable water oxidation, *Angew. Chem. Int. Ed. Engl.* (2023), e202217815, <https://doi.org/10.1002/anie.202217815>.
 - [31] P. Gao, Z. Chen, Y.X. Gong, R. Zhang, H. Liu, P. Tang, X.H. Chen, S. Passerini, J. L. Liu, The role of cation vacancies in electrode materials for enhanced electrochemical energy storage: synthesis, advanced characterization, and fundamentals, *Adv. Energy Mater.* 10 (2020), 1903780, <https://doi.org/10.1002/aenm.201903780>.
 - [32] J. Zheng, X. Peng, Z. Xu, J. Gong, Z. Wang, Cationic defect engineering in spinel NiCo_2O_4 for enhanced electrocatalytic oxygen evolution, *ACS Catal.* 12 (2022) 10245–10254, <https://doi.org/10.1021/acscatal.2c01825>.
 - [33] S.Y. Guan, L.L. An, S. Ashraf, L.N. Zhang, B.Z. Liu, Y.P. Fan, B.J. Li, Oxygen vacancy excites Co_3O_4 nanocrystals embedded into carbon nitride for accelerated hydrogen generation, *Appl. Catal. B* 269 (2020), 118775, <https://doi.org/10.1016/j.apcatb.2020.118775>.
 - [34] T. Koketsu, J. Ma, B.J. Morgan, M. Body, C. Legein, W. Dachraoui, M. Giannini, A. Demortière, M. Salanne, F. Dardozio, H. Groult, O.J. Borkiewicz, K.W. Chapman, P. Strasser, D. Dambournet, Reversible magnesium and aluminium ions insertion in cation-deficient anatase TiO_2 , *Nat. Mater.* 16 (2017) 1142–1148, <https://doi.org/10.1038/nmat4976>.
 - [35] L. Ji, J. Wang, X. Teng, T.J. Meyer, Z. Chen, CoP nanoframes as bifunctional electrocatalysts for efficient overall water splitting, *ACS Catal.* 10 (2020) 412–419, <https://doi.org/10.1021/acscatal.9b03623>.
 - [36] F. Zhou, R.H. Wang, S.C. He, X. Liu, S.Q. Liu, H.Z. Shao, X.P. Liu, Z. Xiao, J.W. Liu, Defect-rich hierarchical porous Mn-doped CoP hollow microspheres accelerate polysulfide conversion, *Adv. Funct. Mater.* 33 (2023), 2211124, <https://doi.org/10.1002/adfm.202211124>.
 - [37] C. Yuan, T. Xu, M. Guo, T. Zhang, X. Yu, Cation/anion-doping induced electronic structure regulation strategy to boost the catalytic hydrogen evolution from ammonia borane hydrolysis, *Appl. Catal. B* 321 (2023), 122044, <https://doi.org/10.1016/j.apcatb.2022.122044>.
 - [38] W. Zhang, N. Han, J. Luo, X. Han, S. Feng, W. Guo, S. Xie, Z. Zhou, P. Subramanian, K. Wan, J. Arbiol, C. Zhang, S. Liu, M. Xu, X. Zhang, J. Fransaer, Critical role of phosphorus in hollow structures cobalt-based phosphides as bifunctional catalysts for water splitting, *Small* 18 (2022), e2103561, <https://doi.org/10.1002/smll.202103561>.
 - [39] Y. Meng, Q. Sun, T. Zhang, J. Zhang, Z. Dong, Y. Ma, Z. Wu, H. Wang, X. Bao, Q. Sun, J. Yu, Cobalt-promoted noble-metal catalysts for efficient hydrogen generation from ammonia borane hydrolysis, *J. Am. Chem. Soc.* 145 (2023) 5486–5495, <https://doi.org/10.1021/jacs.3c00047>.
 - [40] T. Xu, D. Jiao, L. Zhang, H. Zhang, L. Zheng, D.J. Singh, J. Zhao, W. Zheng, X. Cui, Br-induced P-poor defective nickel phosphide for highly efficient overall water splitting, *Appl. Catal. B* 316 (2022), 121686, <https://doi.org/10.1016/j.apcatb.2022.121686>.
 - [41] Z. Zhou, Y. Kong, H. Tan, Q. Huang, C. Wang, Z. Pei, H. Wang, Y. Liu, Y. Wang, S. Li, X. Liao, W. Yan, S. Zhao, Cation-vacancy-enriched nickel phosphide for efficient electrosynthesis of hydrogen peroxides, *Adv. Mater.* 34 (2022), e2106541, <https://doi.org/10.1002/adma.202106541>.
 - [42] O. Akdim, U.B. Demirci, P. Miele, Deactivation and reactivation of cobalt in hydrolysis of sodium borohydride, *Int. J. Hydrog. Energy* 36 (2011) 13669–13675, <https://doi.org/10.1016/j.ijhydene.2011.07.125>.
 - [43] W. Chen, J. Ji, X. Feng, X. Duan, G. Qian, P. Li, X. Zhou, D. Chen, W. Yuan, Mechanistic insight into size-dependent activity and durability in Pt/CNT catalyzed hydrolytic dehydrogenation of ammonia borane, *J. Am. Chem. Soc.* 136 (2014) 16736–16739, <https://doi.org/10.1021/ja509778y>.
 - [44] S. Chen, B. Gong, J. Gu, Y. Lin, B. Yang, Q. Gu, R. Jin, Q. Liu, W. Ying, X. Shi, W. Xu, L. Cai, Y. Li, Z. Sun, S. Wei, W. Zhang, J. Lu, Dehydrogenation of ammonia borane by platinum-nickel dimers: regulation of heteroatom interspace boosts bifunctional synergistic catalysis, *Angew. Chem. Int. Ed. Engl.* 61 (2022), e202211919, <https://doi.org/10.1002/anie.202211919>.
 - [45] Y. Li, W. Wang, M. Cheng, Y. Feng, X. Han, Q. Qian, Y. Zhu, G. Zhang, Arming Ru with oxygen vacancy enriched RuO_2 sub-nanometer skin activates superior bifunctionality for pH-universal overall water splitting, *Adv. Mater.* (2023), e2206351, <https://doi.org/10.1002/adma.202206351>.
 - [46] S. Masuda, K. Shun, K. Mori, Y. Kuwahara, H. Yamashita, Synthesis of a binary alloy nanoparticle catalyst with an immiscible combination of Rh and Cu assisted by hydrogen spillover on a TiO_2 support, *Chem. Sci.* 11 (2020) 4194–4203, <https://doi.org/10.1039/c9sc05612b>.
 - [47] Z. Li, T. He, L. Liu, W. Chen, M. Zhang, G. Wu, P. Chen, Covalent triazine framework supported non-noble metal nanoparticles with superior activity for catalytic hydrolysis of ammonia borane: from mechanistic study to catalyst design, *Chem. Sci.* 8 (2017) 781–788, <https://doi.org/10.1039/c6sc02456d>.
 - [48] H. Lv, R. Wei, X. Guo, L. Sun, B. Liu, Synergistic catalysis of binary RuP nanoclusters on nitrogen-functionalized hollow mesoporous carbon in hydrogen

- production from the hydrolysis of ammonia borane, *J. Phys. Chem. Lett.* 12 (2021) 696–703, <https://doi.org/10.1021/acs.jpclett.0c03547>.
- [49] Y. Wang, X. Li, Z. Huang, H. Wang, Z. Chen, J. Zhang, X. Zheng, Y. Deng, W. Hu, Amorphous Mo-doped $\text{NiS}_{0.5}\text{Se}_{0.5}$ Nanosheets@Crystalline $\text{NiS}_{0.5}\text{Se}_{0.5}$ nanorods for high current-density electrocatalytic water splitting in neutral media, *Angew. Chem. Int. Ed. Engl.* 62 (2023), e202215256, <https://doi.org/10.1002/anie.202215256>.
- [50] Q. Hu, K. Gao, X. Wang, H. Zheng, J. Cao, L. Mi, Q. Huo, H. Yang, J. Liu, C. He, Subnanometric Ru clusters with upshifted D band center improve performance for alkaline hydrogen evolution reaction, *Nat. Commun.* 13 (2022), 3958, <https://doi.org/10.1038/s41467-022-31660-2>.